

Cyclotron and spin resonance in electron inversion layers on InSb

U. Merkt, M. Horst, T. Evelbauer,* and J. P. Kotthaus

Institut für Angewandte Physik, Universität Hamburg, Jungiusstrasse 11, D-2000 Hamburg 36, West Germany

(Received 14 April 1986)

Cyclotron and electron spin resonance in inversion layers on InSb are studied by far-infrared laser and Fourier-transform spectroscopy. For the interpretation of the optical spectra the occupancies of electric subbands in magnetic fields have been derived from Shubnikov–de Haas measurements. Cyclotron masses and effective Landé g factors are given as a function of inversion electron density and of cyclotron energy, i.e., magnetic field. We emphasize nonparabolic and polaron effects and discuss the experimental results with a three-level model in magnetic fields. Since until present no self-consistent calculations in the presence of magnetic fields exist for InSb, we employ the triangular-well approximation for the electrostatic surface potential to obtain a qualitative description of our experiments. At weak magnetic fields good quantitative agreement is obtained between experiments and existing Hartree calculations performed in the absence of magnetic fields.

I. INTRODUCTION

Quasi-two-dimensional (2D) electron systems as realized in space-charge layers on semiconductors have been extensively studied with spectroscopic methods on various materials in recent years.^{1–4} Two-dimensional electron systems on InSb are distinct from the most frequently studied standard systems, namely, metal-oxide-semiconductor (MOS) structures on Si and GaAs-Ga_{1-x}Al_xAs heterostructures. InSb is a narrow-gap semiconductor with a small conduction band mass and strong spin-orbit interaction.⁵ Since InSb is a polar semiconductor, the interaction of quasi-two-dimensional electrons and optical phonons is important in this material.

As a consequence of its narrow gap, the conduction band of InSb is strongly nonparabolic. Both, in the bulk and at an interface, this leads to a cyclotron effective mass that strongly increases with electron density and to an effective Landé g factor that decreases correspondingly. The small effective mass implies a low 2D density of states. Consequently, several subbands are occupied at surface electron densities $n_s \lesssim 5 \times 10^{12} \text{ cm}^{-2}$ that can be attained experimentally.^{6,7}

The polar nature of InSb allows us to study the interaction of optical phonons with quasi-two-dimensional electrons, i.e., polarons. Previously, this polar interaction has been investigated by the magnetophonon effect in GaAs-Ga_{1-x}Al_xAs heterostructures⁸ or by the electrophonon effect on InSb,⁹ i.e., by phonon-induced intersubband resonances. The most significant effect of the polar interaction, however, is the so-called resonant magnetopolaron that is detected as a discontinuity of the cyclotron mass when the cyclotron energy is approximately equal to the optical-phonon energies. Both, three-dimensional¹⁰ and two-dimensional¹¹ resonant magnetopolarons have first been found on InSb. In GaAs, resonant magnetopolarons were only recently detected in the bulk¹² and have not yet been observed in a 2D electron gas of, e.g., GaAs-Ga_{1-x}Al_xAs heterostructures.^{13,14}

Two-dimensional electron systems on InSb have been studied in MOS structures or, more generally, metal-

insulator-semiconductor (MIS) structures. Early transport measurements in inversion and accumulation layers on n -type InSb employed Mylar insulators, but did not reveal effects of surface quantization.¹⁵ Such effects were first observed through Shubnikov–de Haas oscillations in the surface conductivity on p -type InSb.¹⁶ The oscillations have been attributed to the ground and to the first excited subband. Subsequently, cyclotron resonance,¹⁷ electric dipole-induced spin resonance,¹⁸ and intersubband resonance^{19,20} of inversion electrons have been observed and studied.

Theories on 2D electron systems on narrow-gap semiconductors^{21–25} focused on effects of nonparabolicity, on the possibility of tunneling from the conduction to the valence band,^{21,23} and on the lifting of the spin degeneracy of electric subbands caused by the presence of the asymmetric surface potential.²³ Many-body effects such as exchange and correlation could be neglected because of the small density of states.²¹ However, magnetic fields have not been included yet in a self-consistent multiband model that properly accounts for electrons on narrow-gap semiconductors.

In this paper, we review our work on magnetotransport and magneto-optics of inversion layers on InSb. In Sec. II we calculate the subband structure in magnetic fields with a three-level model in the triangular-well approximation (Sec. II A) and give a brief account of the evaluation methods of the optical experiments (Sec. II B). In Sec. III we present some details of sample preparation and experimental methods. Shubnikov–de Haas measurements, cyclotron resonance, and electron spin resonance are discussed in Sec. IV. We conclude with a summary in Sec. V.

II. THEORETICAL CONSIDERATIONS

A. Three-level model in a magnetic field

A qualitative description for electron inversion layers on narrow-gap semiconductors in quantizing magnetic fields is obtained by a three-level model in the triangular-well approximation of the electrostatic potential.^{24,25} In

this model, the effects of nonparabolicity due to the proximity of the valence and the conduction band and the large spin-orbit interaction in InSb are taken into account. Since the triangular-well potential is not a self-consistent one, only approximate values for electric subband and cyclotron energies can be expected. However, simple expressions are obtained that can easily be evaluated and that provide a good physical picture of the surface band structure in magnetic fields. No effort has been made to calculate the inherent spin splitting caused by the asymmetric surface potential since we are concerned with relatively strong magnetic fields that itself cause much larger spin splittings of the energy levels. The inherent spin splitting is most interesting in the absence of magnetic fields²⁶ and has previously been calculated for inversion layers on InSb.²³

The eigenenergies $E = E_{i,n}$ (i subband index, n Landau index) are calculated from the transcendental equation²⁴

$$(a+b)a^{1/2}b^{1/2} + \frac{1}{2}(a-b)^2 \ln \left[\frac{b^{1/2}-a^{1/2}}{b^{1/2}+a^{1/2}} \right] = \left[\frac{E_g}{2m_0^*} \right]^{1/2} 4\pi e \hbar F_s \left(i + \frac{3}{4} \right), \quad (1)$$

where

$$a = E - E_{||}, \quad b = E + E_{||} + E_g, \quad (2)$$

and

$$E_{||} = \left\{ (E_g/2)^2 + E_g \left[\hbar \omega_c \left(n + \frac{1}{2} \right) \pm \frac{1}{2} \mu_B g_0^* B \right] \right\}^{1/2} - E_g/2. \quad (3)$$

The zero of the energy scale is chosen at the conduction-band edge. In the above equations, $E_g = 236$ meV is the gap energy, $\omega_c = eB/m_0^*$ the cyclotron frequency, $m_0^* = 0.0139m_e$ the effective mass with the free-electron mass m_e , and $g_0^* = -51$ the effective Landé factor. The effective mass and the effective Landé factor are both taken at the conduction-band edge. The surface electric field F_s is treated as an adjustable parameter.

Figure 1 shows spin-split Landau levels $E_{i,n}$ of three electric subbands i versus magnetic field. Effects of nonparabolicity in magnetic fields are obvious: the energy of a particular Landau level increases less than linearly with magnetic field and the spacing between adjacent Landau levels (cyclotron energy) decreases when the Landau index n^\pm is increased at a fixed magnetic field. Both effects are different in different electric subbands and, therefore, the cyclotron energy $E_{i,n+1} - E_{i,n}$ depends on magnetic field, on Landau index n^\pm , and on subband index i . In the following, we use the notation n^\pm for $i=0$, (n^\pm) for $i=1$, and $[n^\pm]$ for $i=2$.

From the cyclotron energy a cyclotron mass

$$m_{i,n}^* = \frac{e \hbar B}{E_{i,n+1} - E_{i,n}} \quad (4)$$

can be calculated. Cyclotron masses for two electron densities n_s are given in Fig. 2 versus cyclotron energy to enable comparison with similar experimental figures.¹¹ The masses are only depicted in that range of cyclotron ener-

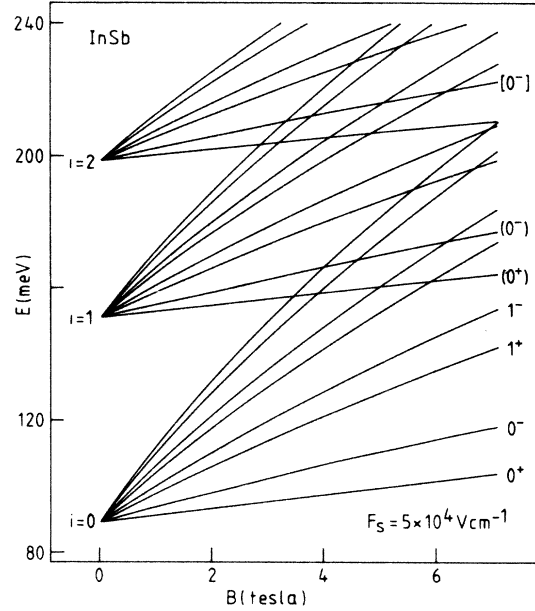


FIG. 1. Spin-split Landau levels n^\pm of three electric subbands $i=0,1,2$. The energies were calculated with a three-level $\mathbf{k} \cdot \mathbf{p}$ model in the triangular-well approximation ($F_s = 5 \times 10^4$ V cm⁻¹) for InSb band parameters ($m_0^* = 0.0139m_e$, $E_g = 236$ meV, $g_0^* = -51$).

gies where the corresponding transitions are possible, i.e., when there are filled states in the initial and empty states in the final Landau level. The filling factors of the Landau levels at a fixed magnetic field are easily obtained

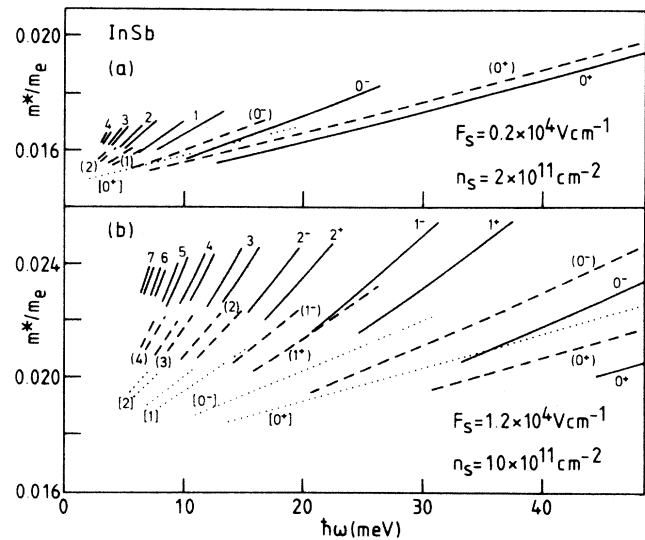


FIG. 2. Apparent cyclotron masses calculated with a three-level $\mathbf{k} \cdot \mathbf{p}$ model in the triangular-well approximation for (a) $n_s = 2 \times 10^{11}$ cm⁻² and (b) $n_s = 10 \times 10^{11}$ cm⁻². The masses for various subbands i are indicated by their Landau indices: n^\pm for $i=0$, (n^\pm) for $i=1$, and $[n^\pm]$ for $i=2$. The masses are only depicted when the corresponding transitions $n^\pm \rightarrow (n+1)^\pm$ are possible.

from figures like Fig. 1 and from the density of states eB/h of a 2D Landau level.

In Fig. 2(a) we have chosen a low electron density $n_s = 2 \times 10^{11} \text{ cm}^{-2}$. The magnetic quantum limit where only the spin-up level 0^+ of the ground electric subband (solid line) is occupied is then reached at $\hbar\omega_c = 48.8 \text{ meV}$ ($B = 8.27 \text{ T}$). Below this energy we also expect the resonance $(0^+) \rightarrow (1^+)$ in the first excited subband (dashed line). Below $\hbar\omega_c = 19 \text{ meV}$ cyclotron resonance $[0^+] \rightarrow [1^+]$ in the $i=2$ subband becomes possible, but not at all cyclotron energies (the dotted line is interrupted twice) since the $[0^+]$ level becomes depopulated.

The situation is even more complicated at the higher electron density $n_s = 10^{12} \text{ cm}^{-2}$ shown in Fig. 2(b). However, when the magnetic field is small ($\hbar\omega_c \rightarrow 0$) cyclotron masses in a particular electric subband i become independent of Landau index n^\pm and cyclotron energy. In this quasiclassical limit we obtain the electric subband masses ($B=0$) that are also obtained from the relation

$$1/m_i^* = \hbar^{-2} k_{\parallel}^{-1} \partial E_i / \partial k_{\parallel},$$

where k_{\parallel} is the 2D momentum parallel to the interface. Strictly speaking, only in this limit it is meaningful to give cyclotron masses m_i^* for various electric subbands without specifying the Landau index n^\pm and the cyclotron energy (or magnetic field).²⁷

B. Evaluation of the experimental spectra

In the experiments we measure the relative change of transmittance $\Delta T/T$ or reflectance $\Delta R/R$ caused by the inversion electrons. In case of transmittance one has

$$\frac{\Delta T}{T} = \frac{T(V_g) - T(V_t)}{T(V_t)}, \quad (5)$$

where $T(V_g)$ and $T(V_t)$ are the transmittances through the sample at the gate voltage V_g and at the threshold voltage V_t (see Sec. III), respectively. Correspondingly, the relative change of reflectance is determined.

In most of the experiments presented here, cyclotron resonance maxima can be read directly from the experimental traces. However, if electrons with relatively low surface mobilities μ_s in more than one subband are involved, we have to model the experimental spectra to extract the resonance positions. Model calculations were also employed to understand the signals when cyclotron resonance interferes with the reststrahlen band.

In our model, the frequency-dependent conductivity $\hat{\sigma}_s$ of the inversion electrons is represented by the classical Drude expression

$$\hat{\sigma}_s(\omega, B) = \sum_i \frac{en_i \mu_i}{1 - j(\omega - \omega_{ci})\tau_i}, \quad (6)$$

where n_i is the electron density, $\omega_{ci} = eB/m_i^*$ the cyclotron frequency, $\mu_i = e\tau_i/m_i^*$ an effective mobility, and τ_i the relaxation time in a particular subband i , respectively.

For the optical phonons the bulk dielectric function

$$\hat{\kappa}(\omega) = \kappa_1 + j\kappa_2 = \kappa_\infty + \frac{(\kappa_0 - \kappa_\infty)\omega_{\text{TO}}^2}{\omega_{\text{TO}}^2 - \omega^2 - j\Gamma\omega} \quad (7)$$

is assumed. In Eq. (7) κ_0 and κ_∞ are the static and the high-frequency dielectric constants, respectively, ω_{TO} the frequency of the TO phonons,^{28,29} and Γ the phonon damping parameter.

The relative changes of transmittance and reflectance are numerically calculated with an optical layer model based on Eqs. (5)–(7). The layer model accounts for the occupation of more than one subband and for the polarization of the incident light. The exact Fresnel formulas used in the model calculations are principally simple, but lengthy and not very illustrative.

For wedged samples without interference effects we can give simple approximate expressions for the low-signal limit

$$\frac{\Delta T}{T} \simeq -2 \text{Re} \left[\frac{\hat{\sigma}_s/Y_0}{\sqrt{\hat{\kappa}} + 1} \right], \quad (8a)$$

$$\frac{\Delta R}{R} \simeq +4 \text{Re} \left[\frac{\hat{\sigma}_s/Y_0}{\hat{\kappa} - 1} \right], \quad (8b)$$

where

$$Y_0 = (\epsilon_0/\mu_0)^{1/2} = (377\Omega)^{-1}$$

is the wave admittance of the vacuum. If necessary, the sheet conductivity of the gate metal σ_\square can be included by adding σ_\square/Y_0 in the denominators of Eqs. (8) and 8(b). Well away from the reststrahlen band $\kappa_2 \simeq 0$ and Eq. 8(a) reduces to a previously given expression.³⁰

Figure 3(a) shows an experimental transmittance spectrum (solid line) and its theoretical description (dashed line) assuming the occupation of two electric subbands (dotted lines $i=0,1$). The experimental spectrum has been measured at a fixed laser energy $\hbar\omega = 17.6 \text{ meV}$ in a sweep of the magnetic field B .

If we extract the subband densities n_i from an analysis of the Shubnikov–de Haas oscillations of the static conductivity (see Sec. IV A) we can get satisfactory agreement between the experimental and the fitted spectra and thus extract cyclotron masses from these classical fits. In general, however, classical fits only approximately describe the experimental spectra. When quantum oscillations² cause strong structure on the experimental spectra a classical fit alone may cause misinterpretation. In such cases additional information was used such as the temperature dependence of the spectra²⁷ or the analysis of Shubnikov–de Haas oscillations to identify subband cyclotron resonances.

Figure 3(b) shows a reflectance spectrum obtained with a Fourier transform spectrometer at a fixed magnetic field. The theoretical fit has been obtained by a superposition of three Lorentzian lines. The resonances labeled $i=0,1$ are the main subband cyclotron resonances, that are also observed in sweeps of the magnetic field at fixed laser energies $\hbar\omega$. The structure at wave number $\tilde{\nu} = 229 \text{ cm}^{-1}$ (see arrow) is interpreted as an additional cyclotron resonance transition between higher Landau levels in the ground subband $i=0$.

Most interesting is the change of the relative reflectance $\Delta R/R$ inside the reststrahlen band ($\tilde{\nu}_{\text{TO}} = 183 \text{ cm}^{-1}$,

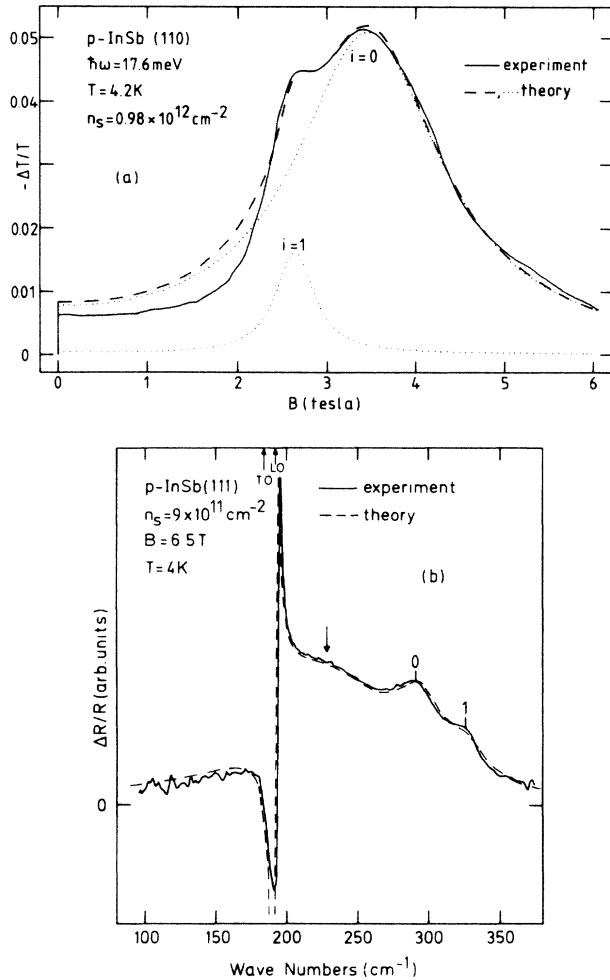


FIG. 3. Experimental and theoretical line shapes. The transmittance spectrum (a) was taken at a fixed laser energy $\hbar\omega$ in a sweep of the magnetic field and is described by cyclotron resonances in two subbands ($i=0,1$). The dashed line gives the theoretical fit and the dotted lines give the contributions from individual electric subbands. The reflectance spectrum (b) was taken with a Fourier transform spectrometer and is described by two cyclotron resonances ($i=0,1$) and an additional cyclotron resonance transition between higher Landau levels in the ground subband (see arrow).

$\tilde{\nu}_{\text{LO}} = 194 \text{ cm}^{-1}$, see Ref. 29). There is a sharp negative minimum at 190 cm^{-1} and a sharp positive maximum at about 195 cm^{-1} . These structures can be explained with Eq. 8(b), if this equation is explicitly written for the cyclotron-active polarization and one single cyclotron resonance

$$\frac{\Delta R}{R} \simeq + \frac{4}{(\kappa_1 - 1)^2 + \kappa_2^2} \frac{\sigma_0/Y_0}{1 + (\omega - \omega_c)^2 \tau^2} \times [(\kappa_1 - 1) + \kappa_2(\omega - \omega_c)\tau], \quad (9)$$

where $\sigma_0 = en\mu$. The behavior inside the reststrahlen band is mainly determined by the term $\kappa_1 - 1$, that is negative inside the reststrahlen band. Just above the LO-phonon

frequency, $\kappa_1 - 1$ vanishes and the signal becomes strong (except for $\omega = \omega_c$). Physically, the negative signals are explained by the fact, that inside the reststrahlen band the metallic inversion layer can “match” the vacuum to the totally reflecting semiconductor.

III. EXPERIMENTAL DETAILS

The experiments were performed on *p*-type ($N_A \sim 3 \times 10^{14} \text{ cm}^{-3}$) InSb samples with SiO_2 gate oxides and semitransparent NiCr gate contacts. The commercially available InSb wafers (MCP Electronics) were cut into platelets of typical dimensions $6 \times 5 \times 0.5 \text{ mm}^3$. For experiments near the reststrahlen band we also used thinner substrates ($d \simeq 0.2 \text{ mm}$). A mechanical polish with alumina powder ($15\text{--}0.3 \mu\text{m}$) was followed by a chemical etch polish in a bromine in methanol solution. The concentration of bromine that was necessary to produce damage-free layers was different for the different principal surfaces: for the In-rich (111)*A* and Sb-rich (111)*B* surfaces³¹ 0.0025% Br_2 , but 0.05% Br_2 for the (100) and (110) surfaces. Etching was stopped by rinsing in methanol and blowing dry with nitrogen. To remove organic residues, the surfaces were cleaned in an oxygen plasma prior to the deposition of the gate insulator. The SiO_2 gate insulator ($d_{\text{ox}} \simeq 200 \text{ nm}$) was deposited by a plasma-enhanced chemical-vapor-deposition (CVD) process³² at a substrate temperature of about 80°C . To enable far-infrared experiments thin NiCr films ($d \simeq 3 \text{ nm}$) with areas $A \simeq 8 \text{ mm}^2$ were evaporated as gate contacts. Substrate contacts were achieved with silver paint. For the magnetotransport measurements, two thick aluminum stripes ($d \simeq 100 \text{ nm}$) were evaporated onto the thin NiCr to act as capacitively coupled source and drain contacts³³ at radio frequencies ($\nu \simeq 20 \text{ MHz}$).

MOS structures were prepared on all principal surfaces and were characterized by capacitance-voltage (*C-V*) curves, magnetoconductance, and Shubnikov–de Haas (SdH) measurements (see Sec. IV A). Conductivity thresholds V_t typically range between -10 and -2 V . Except on the (111)*A* surface, nearly all ($>95\%$) electrons $n_{\text{ind}} = (V_g - V_t)C/eA$ that are induced by the gate voltage V_g are found to be mobile and to occupy inversion layer subbands. Because the threshold in most cases could be determined only within $\Delta V_t \simeq \pm 0.5 \text{ V}$, the determination of the inversion electron density was limited to $\Delta n_s \simeq \pm 5 \times 10^{10} \text{ cm}^{-2}$. The highest surface mobilities $\mu_s \simeq 5 \times 10^4 \text{ cm}^2 \text{ V}^{-1} \text{ s}^{-1}$ were obtained on the (111)*B* surface. However, mobilities $\mu_s \simeq 2.5 \times 10^4 \text{ cm}^2 \text{ V}^{-1} \text{ s}^{-1}$ at $n_s \simeq 10^{12} \text{ cm}^{-2}$ are more typical and are routinely obtained on all principal surfaces.

The spectroscopic experiments were carried out with far-infrared lasers and a Fourier transform spectrometer at liquid-helium temperatures ($T \simeq 4 \text{ K}$) using standard techniques.^{2,34}

IV. RESULTS AND DISCUSSION

A. Shubnikov–de Haas analysis

The occupancies of electric subbands can be determined alone from the periodicity of Shubnikov–de Haas oscilla-

tions in low magnetic fields.^{1,6} In strong magnetic fields, the 2D electron gas becomes totally quantized. Then, the filling of particular spin-split Landau levels n^\pm should be considered. For this, a Landau index n^\pm and a subband index i must be attributed to each Shubnikov–de Haas maximum.

We have analyzed the Shubnikov–de Haas effect on all principal surfaces (100), (110), (111)*A*, and (111)*B*. As an example, derivatives of the inversion channel conductivity with respect to the gate voltage are given in Fig. 4 at various carrier densities for the (110) surface. From the magnetic fields B_n and B_{n+1} of successive maxima or minima, the subband densities n_i can be extracted using the relation

$$B_n^{-1} - B_{n+1}^{-1} = g_s e / n_i h, \quad (10)$$

where g_s is the spin degeneracy.¹

Results for all three surfaces are depicted in Fig. 5(a) together with theoretical values (dashed line, Ref. 21). Shubnikov–de Haas oscillations of up to four subbands are observed. The theoretical values which are calculated in the absence of magnetic fields are slightly different in spin-up and spin-down electrons as a consequence of in-

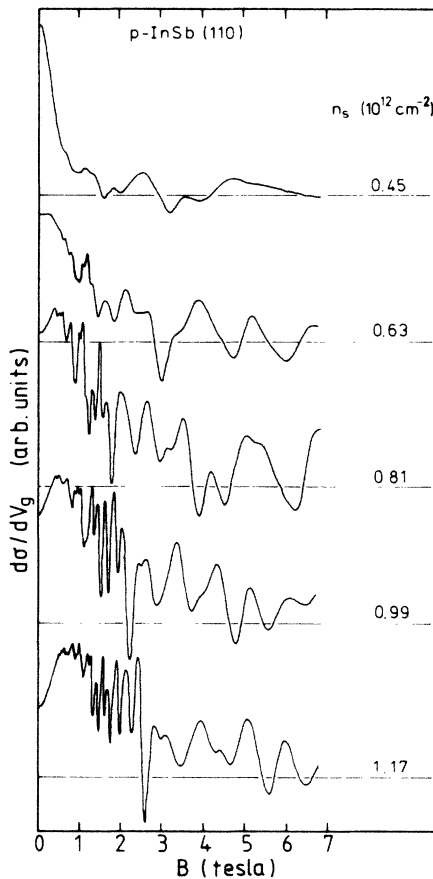


FIG. 4. Shubnikov–de Haas oscillations in the conductivity of inversion electrons on InSb (110) for various electron densities n_s , measured with capacitive source-drain contacts at a frequency of 20 MHz.

version asymmetry. This difference has been averaged out for the figure. Our experimental values agree with the ones of Därr *et al.*⁶ obtained for densities up to $n_s \approx 1 \times 10^{12} \text{ cm}^{-2}$ on the (111) surface. Subband occupancies on all three surfaces agree among each other and with theory. Figure 5(a) also demonstrates, that nearly all ($\geq 95\%$) induced electrons (solid line) contribute to the total 2D density n_s , which is the sum over all subband densities n_i . In the following we therefore set $n_{\text{ind}} = n_s$, i.e., we determine the total inversion electron density from the oxide capacitance and the threshold voltage.

The experimental subband densities indicate that the subband structure is the same on all surfaces. This is simply explained by the isotropy of the bulk InSb band struc-

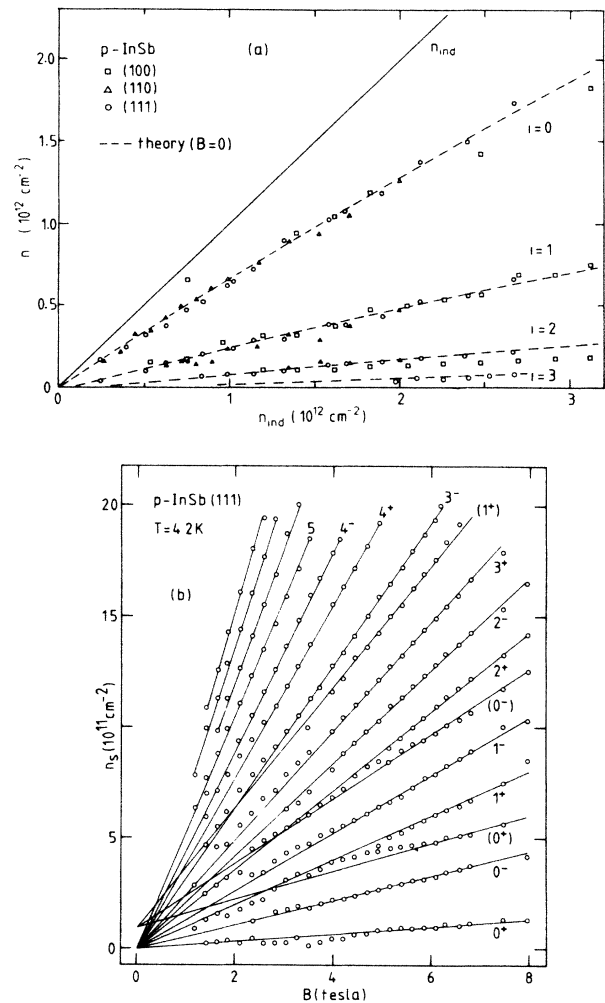


FIG. 5. (a) Subband densities n_i in four electric subbands ($i=0-3$) vs induced electron density n_{ind} . The subband densities n_i and the induced density n_{ind} were determined from Shubnikov–de Haas oscillations and from the oxide capacitance, respectively. The dashed lines are theoretical values taken from Ref. 21. (b) Maxima of Shubnikov–de Haas oscillations (fan chart) indicated by Landau indices of the ground subband n^\pm and the first excited subband (n^\pm). Solid lines are guides for the eye only.

ture: The same subband states are obtained when a Fermi sphere is projected onto an arbitrary surface. This picture does not take into account the chemical nature of the surface. The quality of the semiconductor-oxide interface is different on different surfaces, as is evidenced by different surface mobilities (see Sec. III). Since the (110) and the (111)*B* surfaces show the highest mobilities and since we found no evidence for different behavior in the optical experiments, we mostly restrict our discussion to results obtained on those surfaces.

Figure 5(b) presents a so-called "fan chart" for inversion layers on InSb.³⁵ In the fan chart the electron densities n_s at which a particular Landau level (n^\pm, i) of an electric subband i shows a Shubnikov-de Haas maximum in the derivative $d\sigma/dV_g$ are given versus magnetic field B . The fan chart is very useful in the interpretation of optical measurements, since it gives the possible initial and final states at a particular density. For example, at $B=5$ T and $n_s=5 \times 10^{11}$ cm⁻², the levels ($0^\pm, 0$) and ($1^\pm, 0$) are expected to be completely filled whereas the levels ($1^-, 0$) and ($0^+, 1$) are partially filled.

B. Cyclotron resonance

1. Experimental spectra

Experimental cyclotron spectra on InSb show a variety of structures that depend on electron density and magnetic field or cyclotron energy $\hbar\omega_c$. In this section, we illustrate this with some typical examples. Figures 6 and 7 show sweeps of the magnetic field at fixed laser energies $\hbar\omega$, Figs. 8 and 9 show frequency-domain studies. We are going to discuss both, magnetic and dispersive spectroscopy, since they complement each other. Whereas resonance positions can be extracted more precisely from laser spectra, since signal-to-noise ratio is higher, the interpretation of frequency-domain studies is more straightforward, since the surface band structure is kept constant in the fixed magnetic field.

Figure 6 shows laser spectra for the energy $\hbar\omega=17.6$ meV at various electron densities n_s . Subband cyclotron resonance is observed in three subbands ($i=0,1,2$) and cyclotron masses $m_i^* = eB_i/\omega$ can only directly be read from the traces at intermediate densities [(0.71–1.49) $\times 10^{12}$ cm⁻²]. At higher densities quantum oscillations and the absorption of bound holes in the *p*-type substrate (see dashes) prevent direct reading of the resonance positions and they must be determined from theoretical fits (Sec. II B). At lower densities the electron mobility is not sufficiently high enough to separate clearly cyclotron resonance in the ground and first excited subband. In the figure the more pronounced quantum oscillations are marked by arrows. These quantum oscillations were identified by their magnetic field position and by the fact that they smear out at temperatures $kT \sim \hbar\omega_c$ (see Ref. 27).

In spectra at still lower laser energies, subband cyclotron resonances usually are not clearly resolved. However, such traces ($\hbar\omega \ll E_F$) are rather well described by classical theory (Sec. II B) and cyclotron masses are obtained from fits that are based on the experimentally determined subband densities n_i shown in Fig. 5(a). The cyclotron masses are discussed in Sec. IV B 2. In addition to the cy-

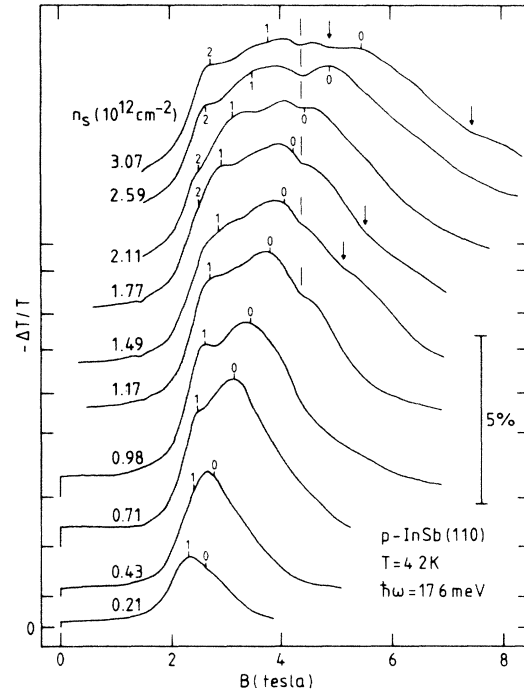


FIG. 6. Experimental cyclotron spectra at the laser energy $\hbar\omega=17.6$ meV and various electron densities n_s . The resonance positions of subband cyclotron resonances as obtained from theoretical fits are indicated ($i=0,1,2$). The arrows mark more pronounced quantum oscillations, the dashes, cyclotron resonance of bound holes in the *p*-type substrate.

clotron masses m_i^* , the relaxation times τ_i act as fit parameters. Typically, in the ground subband $\tau_0 \approx 2 \times 10^{-13}$ s is obtained at the density $n_s = 10^{12}$ cm⁻². Relaxation times are longer in higher subbands ($\tau_1 \approx 4 \times 10^{-13}$ s, $\tau_2 \approx 5 \times 10^{-13}$ s) and are not very sensitive to the carrier density and to magnetic field except for a broadening just above the LO-phonon energy.³⁶

The definition of a subband cyclotron mass independent of Landau index is not meaningful in strong quantizing magnetic fields since there are distinct Landau transitions (see Sec. II A). This is demonstrated in Fig. 7 with spectra at a relatively high laser energy $\hbar\omega=44.3$ meV. Here only a few Landau levels become occupied since at $B=10$ T the density of states of one Landau level is 2.4×10^{11} cm⁻². Hence the Fermi energy is comparable to the cyclotron energy ($E_F \sim \hbar\omega_c$) and Landau quantization strongly influences the spectra. In a sweep of the magnetic field the Fermi level successively passes through the Landau levels causing quantum oscillations in the absorption of each electric subband.²⁷ Accordingly, experimental resonance positions do not only reflect the energy separation $E_{i,n+1} - E_{i,n}$ but they also reflect the joint density of states when more than one Landau level is occupied in a particular electric subband i . With the quantum oscillations in mind we can qualitatively understand the spectra in Fig. 7.

At the lowest density $n_s = 1.4 \times 10^{11}$ cm⁻² only the ground Landau level 0^+ of the ground electric subband

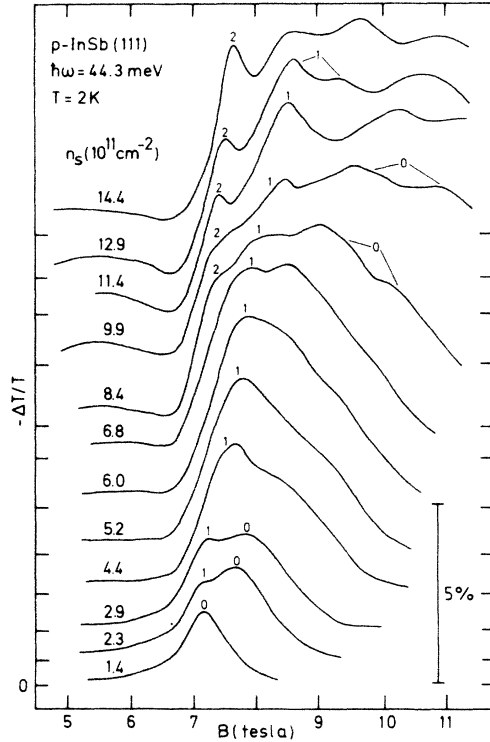


FIG. 7. Experimental cyclotron spectra at the laser energy $\hbar\omega = 44.3$ meV and various electron densities n_s . Cyclotron resonances in the subbands $i=0,1,2$ are indicated where possible.

$i=0$ is occupied at magnetic fields $B \geq 5.8$ T and we obtain a cyclotron mass $m^* = 0.0187m_e$ for the $0^+ \rightarrow 1^+$ transition. This mass is slightly higher than the one of the conduction-band cyclotron resonance³⁷ in bulk n -type InSb ($m^* = 0.0180m_e$), reflecting the influence of the electric field (Sec. II A). At higher densities, the 0^- level becomes populated but we cannot resolve spin-split cyclotron resonances. In addition to the $0 \rightarrow 1$ resonance, the resonance $(0) \rightarrow (1)$ in the subband $i=1$ is observed at a higher density $n_s = 2.3 \times 10^{11} \text{ cm}^{-2}$. The transition $[0^+] \rightarrow [1^+]$ in the third electric subband ($i=2$) is first detected at the density $n_s = 8.4 \times 10^{11} \text{ cm}^{-2}$. It is interesting to note, that in all electric subbands the resonance of the ground Landau level starts approximately at the same resonance magnetic field $B \approx 7.2$ T corresponding to a mass $m^* = 0.0188m_e$.

At densities $n_s \geq 4.4 \times 10^{11} \text{ cm}^{-2}$ the contribution of the ground electric subband becomes relatively broad and is strongly affected by quantum oscillations. We then cannot reliably extract resonance positions since we have no detailed theory of the cyclotron resonance line shapes in such strongly quantizing magnetic fields. However, with the aid of the fan chart we can attribute the oscillations to distinct Landau transitions. For the density $n_s = 9.9 \times 10^{11} \text{ cm}^{-2}$ the two structures at $B = 9.6$ T and $B = 11.0$ T indicated by the subband index $i=0$ arise probably from the $0^- \rightarrow 1^-$ and $0^+ \rightarrow 1^+$ transitions, respectively. We cannot unambiguously identify the structures indicated by the subband index $i=1$ on the

spectrum for the density $12.9 \times 10^{11} \text{ cm}^{-2}$, but they might represent the spin-split $(0^\pm) \rightarrow (1^\pm)$ transition.

The spectra shown in Fig. 8 have been measured with a Fourier transform spectrometer at a fixed magnetic field. Principally, in such experiments quantum oscillations are avoided and resonance maxima of various Landau transitions should appear right at the corresponding Landau energies. However, the mobilities of the present samples are not sufficiently high to resolve all Landau transitions at larger densities n_s in a wider range of frequencies and magnetic fields. This becomes clear from the spectrum for the highest density $n_s = 2.0 \times 10^{12} \text{ cm}^{-2}$ where the resonances of the ground and first excited subband are completely smeared out. However, the spectra in Fig. 8 clearly demonstrate the effect of nonparabolicity at larger magnetic fields. With increasing densities n_s , the resonances shift to lower frequencies, i.e., cyclotron masses in a given subband increase with increasing density.

In Fig. 9 reflectance spectra are shown at various magnetic fields. The origin of the sharp structures inside the reststrahlen band ($183\text{--}194 \text{ cm}^{-1}$) was already explained in Sec. II B. Results obtained from cyclotron resonance in the vicinity of the reststrahlen band (magnetopolarons) will be discussed in Sec. III B 3. Inside the reststrahlen band the position of the cyclotron frequency ω_c can only be obtained from theoretical fits. Only when the complex part of the dielectric constant is small ($\kappa_2 \approx 0$), the cyclotron frequency can directly be read from the traces according to Eq. (4). In the reststrahlen band, cyclotron res-

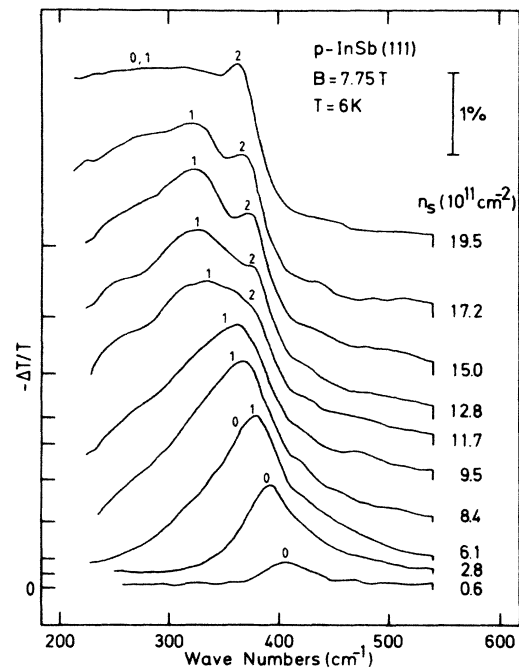


FIG. 8. Cyclotron resonance spectra measured by Fourier transform spectroscopy at a fixed magnetic field and various electron densities n_s . Cyclotron resonances in the subbands $i=0,1,2$ are indicated. At densities $n_s \geq 15 \times 10^{11} \text{ cm}^{-2}$, the pronounced structures at $\tilde{\nu} \approx 370 \text{ cm}^{-1}$ are cyclotron resonances $[0^+] \rightarrow [1^+]$ of the subband $i=2$.

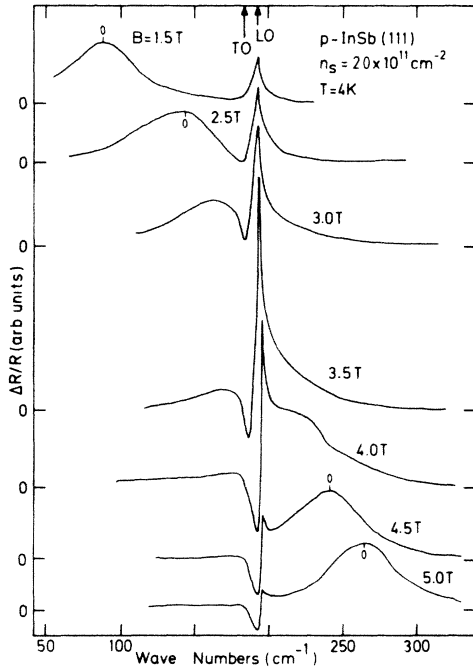


FIG. 9. Reflectance spectra of cyclotron resonance at various magnetic fields below and above the reststrahlen band ($183\text{--}194\text{ cm}^{-1}$). At the low electron density $n_s = 2.0 \times 10^{11}\text{ cm}^{-2}$ the signal is predominantly due to cyclotron resonance in the ground subband $i=0$.

onance is expected to be split by the resonant interaction of optical phonons and electrons.^{10,38} This cannot directly be deduced from our spectra unambiguously, though we found by simulation with Lorentzian profiles that the line shape inside the reststrahlen band is best described assuming two modes. However, in this procedure too many parameters are involved and therefore we rely on direct reading of resonance positions outside the reststrahlen band for the discussion of magnetopolarons in Sec. III B 3.

2. Nonparabolic subband masses

Subband masses that have been extracted from experimental spectra taken at the laser energy $\hbar\omega = 17.6\text{ meV}$ (see Fig. 6) are displayed versus density n_s in Fig. 10. We restrict the extraction and discussion of subband cyclotron masses to this relatively low energy, since it leads to comparatively low resonance magnetic fields ($B \simeq 2\text{--}4\text{ T}$). As was pointed out in Sec. II A, it is only meaningful to extract subband masses in the limit of low magnetic fields ($B \rightarrow 0$). On the other hand, at laser energies much lower than $\hbar\omega = 17.6\text{ meV}$ sharp cyclotron resonance no longer could be observed ($\omega\tau \sim 1$).

The masses in all subbands increase with electron density n_s , reflecting the nonparabolicity of electric subbands on InSb. The increase is different in different subbands and is strongest in the ground subband. These general trends are qualitatively described by the simple triangular-well approximation of the surface electric potential (see Fig. 2). The experimental points show some deviations from monotonic increase caused by the influ-

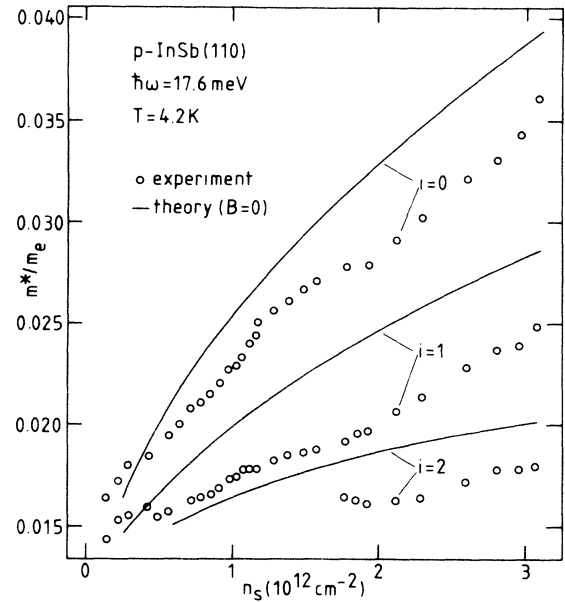


FIG. 10. Subband cyclotron masses vs electron density n_s for three electric subbands ($i=0,1,2$) measured at a fixed laser energy $\hbar\omega$. Solid lines are theoretical values taken from Ref. 21.

ence of quantum oscillations. This effect is most clearly seen for the mass of the ground subband in the density range $n_s \simeq (1\text{--}2) \times 10^{12}\text{ cm}^{-2}$. Measurements on many samples show that the masses are reproducible within about 10% on the density scale and about 5% on the mass scale.

The solid lines are theoretical values taken from Ref. 21. These values have been calculated in the absence of magnetic fields. It is surprising that the theoretical masses are higher than the experimental ones, since one would expect from nonparabolicity that the $B=0$ masses are lower than those at finite magnetic fields. Thus a more complete theory including magnetic field effects is necessary.

Previously published data by Därr *et al.*¹⁷ show qualitatively the same behavior as our data. However, in these experiments a mylar foil was used as insulator and simultaneous Shubnikov–de Haas measurements were not possible. Thus the electron density n_s had to be determined with a large uncertainty (as much as 50%) from the insulator thickness alone.

The experimental masses in Fig. 10 are higher than the band-edge mass of conduction electrons ($m_0^* = 0.0139m_e$) in bulk samples with low doping. It is also interesting to compare subband masses with effective masses in degenerate bulk n -type InSb. At an electron density $n_s = 1 \times 10^{12}\text{ cm}^{-2}$ the width of the ground subband is $a \simeq 100\text{ nm}$ and the density in the ground subband is $n_0 = 0.85 \times 10^{12}\text{ cm}^{-2}$ [see Fig. 5(a)]. This corresponds to a volume density $n_0/a = 0.85 \times 10^{18}\text{ cm}^{-3}$. At this carrier concentration, the InSb bulk mass is $m^* = 0.029m_e$ ($T = 77\text{ K}$, see Ref. 39), whereas in inversion layers the mass in the ground subband is $m^* = 0.025m_e$.

We have also studied cyclotron masses at extremely low

densities $n_s \leq 1 \times 10^{11} \text{ cm}^{-2}$. At such densities we often find at laser energies $\hbar\omega \gtrsim 10 \text{ meV}$ that the cyclotron resonance of the inversion electrons lies in between the bulk conduction band and the bulk impurity cyclotron resonance. At lower laser energies (e.g., $\hbar\omega = 2.9 \text{ meV}$) we even found that the surface resonance ($m^* = 0.0096m_e$) lies well below the bulk impurity resonance ($m^* = 0.0124m_e$ at $\hbar\omega_c = 3.7 \text{ meV}$, see Ref. 37). These observations imply that inversion electrons at low densities feel interface or oxide charges analogously as bulk electrons feel donor charges. Similar localization effects near interfaces have extensively been studied in silicon MOS structures.⁴⁰

3. Magnetopolarons

The interaction of optical phonons with quasi-two-dimensional electrons has recently attracted much interest, both theoretically (see Refs. 41–43) and experimentally (see Refs. 11, 13, 14, and 44–46). Two situations are commonly distinguished: the nonresonant polaron in the absence of a magnetic field or in low magnetic fields and the resonant magnetopolaron in quantizing magnetic fields when the cyclotron energy approximately equals the optical-phonon energy ($\hbar\omega_c \simeq \hbar\omega_{LO}$). The resonant interaction of the cyclotron resonance with the optical phonons causes a coupled mode with two polaron branches. Equivalently, there is a discontinuous change of the apparent cyclotron mass that can easily be detected in cyclotron resonance experiments. Therefore, in most experiments resonant magnetopolarons have been studied (see Refs. 11, 13, 14, and 46). In the nonresonant situation ($\hbar\omega_c \ll \hbar\omega_{LO}$) a polaron mass is difficult to deduce from experiments without ambiguity since band nonparabolicity corrections and polaronic effects are quantitatively similar.^{13,44}

Theoretically it has been found that the polaron mass in the purely 2D limit is enhanced over the three-dimensional (3D) Fröhlich result if screening effects and the finite width of the quasi-two-dimensional electron layer are ignored (see Refs. 38, 43, and 47). In the absence of magnetic fields, the 2D polaron mass renormalization $(\pi\alpha/8)m_0^*$ is enhanced by more than a factor of 2 over the 3D Fröhlich result $(\alpha/6)m_0^*$. In the resonant situation ($n = 0 \rightarrow n = 1$), the splitting of the 2D resonant polaron $\Delta m_{2D}/m = \pm 1/2\pi^{1/2}\alpha^{1/2}$ is enhanced by a factor of about 4 over the three-dimensional result $\Delta m_{3D}/m \simeq \pm(\alpha/2)^{2/3}$ assuming the bulk Fröhlich coupling constant $\alpha = 0.023$. However, it has been shown theoretically for GaAs-Ga_{1-x}Al_xAs heterostructures that wave-function effects and screening effects can strongly decrease this enhancement.⁴⁸ Qualitatively, one expects similar reduction in other quasi-two-dimensional electron systems.

The wave-function effect describes the deviation from the strictly 2D behavior due to the finite width of the wave function perpendicular to the interface. The corresponding form factor for the Fang-Howard variational wave function¹ of the ground subband

$$f(q) = \frac{1}{8} \left[1 + \frac{qa}{3} \right]^{-3} (8 + 3qa + \frac{1}{3}q^2a^2) \quad (11)$$

has been calculated by Das Sarma and Mason.⁴¹ In Eq. (11) a denotes the spread of the wave function, i.e., the thickness of the inversion layer.

Screening of the polar interaction is also important in the degenerate quasi-two-dimensional systems but has not yet been calculated taking fully into account dynamical screening in the presence of strong magnetic fields. An upper limit for the screening effect can be obtained by the static Thomas-Fermi expression $\kappa(q) = 1 + q_{TF}/q$, where $q_{TF} = m_0^*e^2/2\pi\epsilon_0\hbar^2$ is the 2D screening wave vector.¹ A fairly accurate approximation to the polaronic mass enhancement in realistic 2D structures is obtained by multiplying the strictly 2D result by the factor $f(q = \gamma)[\kappa(q = \gamma)]^{-2}$, where $\gamma = (\hbar/2m_0^*\omega_{LO})^{-1/2}$ is the inverse polaron radius.⁴¹

Figure 11 shows cyclotron masses of the first two subbands $i=0,1$ as a function of the cyclotron energy $\hbar\omega_c$ in the vicinity of the reststrahlen band. The masses have been extracted from spectra like those in Fig. 6 (see also Ref. 11). For comparison bulk masses of n -type InSb ($n = 6 \times 10^{13} \text{ cm}^{-3}$) are included. As a result of nonparabolicity, subband masses increase at low densities similar to bulk masses at the low volume density. At higher den-

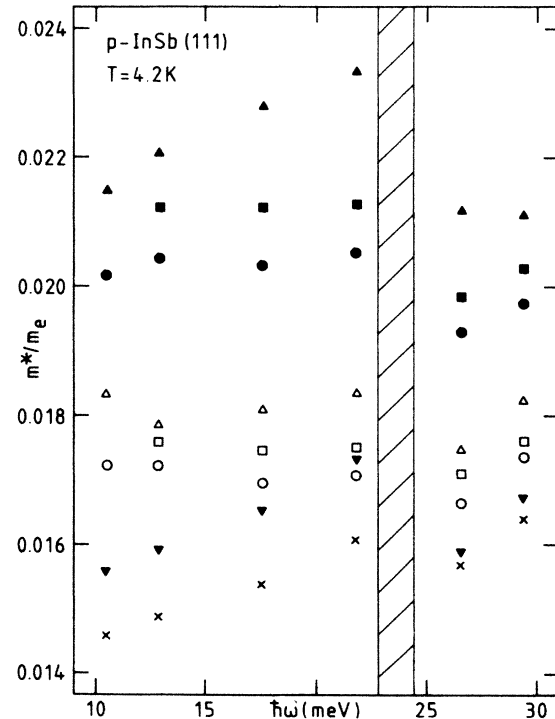


FIG. 11. Discontinuities of cyclotron masses in the vicinity of the reststrahlen band (hatched region) demonstrating the resonant magnetopolaron effect. Results are shown for the ground subband (closed symbols) and the first excited subband (open symbols) at four electron densities n_s : $2.0 \times 10^{11} \text{ cm}^{-2}$ (inverted triangles); $6.4 \times 10^{11} \text{ cm}^{-2}$ (circles); $8.2 \times 10^{11} \text{ cm}^{-2}$ (squares); $10 \times 10^{11} \text{ cm}^{-2}$ (triangles). For comparison, bulk values of n -type InSb are also shown (crosses).

sities the masses are essentially constant, except for the highest density $n_s = 10 \times 10^{11} \text{ cm}^{-2}$ in the ground subband $i=0$. In this case the observed increase might be explained by the fact that we observe the $2^{\pm} \rightarrow 3^{\pm}$ transition in the whole $\hbar\omega_c \approx 10\text{--}20 \text{ meV}$ range (see Fig. 2). Near the reststrahlen band a discontinuous change of the mass is always observed. This is the resonant magnetopolaron effect. In InSb we observe a strong decrease of the apparent cyclotron mass just above the LO-phonon energy. Recent experiments on GaInAs-InP heterostructures report pinning close to the TO-phonon energies.⁴⁶

A convenient experimental measure of the resonant magnetopolaron on InSb is the mass discontinuity between the two laser lines $\hbar\omega = 21.8 \text{ meV}$ and $\hbar\omega = 26.6 \text{ meV}$ that lie closest to the reststrahlen band in our experiments. The figure shows, that the surface polaron effect is enhanced as compared to the bulk effect by a factor of about 3–6.

The resonant polaron effect on InSb has been calculated using a variational model.⁴⁹ Quantitative agreement with our experimental data was obtained, if somewhat lower inversion electron densities than in the experiments were assumed in the calculations. In case of inversion layers on InSb screening and wave-function effects do not seem to reduce the polaron interaction below the bulk value as it was reported for GaAs-Ga_{1-x}Al_xAs heterostructures.¹⁴ Qualitatively, this may be understood from the screening and form-factor arguments discussed above.

In InSb, the subband width $a \approx 150 \text{ \AA}$ at a typical density $n_s = 5 \times 10^{11} \text{ cm}^{-2}$ is quite comparable to the polaron radius $\gamma^{-1} = 105 \text{ \AA}$. This should lead to a reduction of the resonant polaron effect by approximately a factor of 2 via the wave-function effect [see Eq. (11)]. Because the screening length $q_{\text{TF}}^{-1} = 238 \text{ \AA}$ is large, screening is not very effective on InSb. This is particularly true when dynamical screening, which takes into account the dielectric response $\kappa(q, \omega)$ at all frequencies, is applied. Then the reduction of the polaron binding energy and the polaron mass due to screening were found to be much weaker than in the static Thomas-Fermi approach.⁵⁰ Therefore, even if the effects of the finite width of the wave function and screening are included into the strictly 2D polaron effect, we still expect an enhancement of the resonant interaction as it is observed in Fig. 11.

C. Electron spin resonance

Electron spin resonance in inversion layers on InSb (111) is most clearly detected, when the direction of the magnetic field is tilted with respect to the surface normal.¹⁸ The optimum angle between magnetic field and surface normal is about $\theta = 45^\circ$. Whereas it has been argued previously¹⁸ that electron spin resonance should vanish in the corresponding bulk configuration it has been shown recently⁵¹ that there is in fact a finite matrix element. In addition, the strong gradient of the surface electric potential may enhance the effective spin-orbit interaction and modify the selection rules.

Figure 12 shows transmittance spectra in tilted magnetic fields ($\theta = 45^\circ$) at various electron densities. The structures at $B \approx 4.5 \text{ T}$ are caused by electron spin resonance.

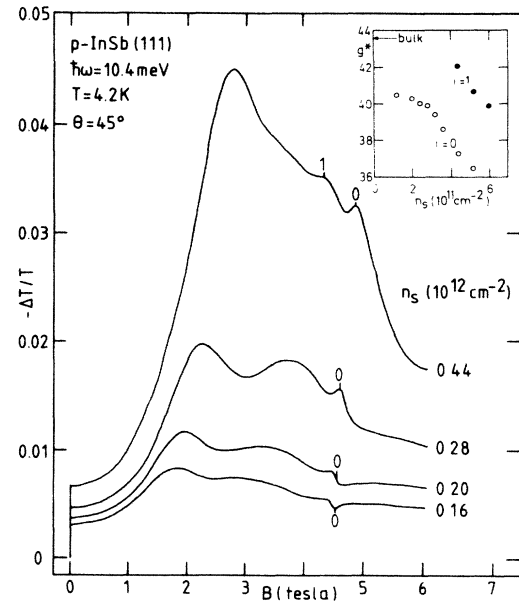


FIG. 12. Cyclotron and electron spin resonance at the laser energy $\hbar\omega = 10.4 \text{ meV}$ and various electron densities n_s . The magnetic field is tilted with respect to the surface normal ($\theta = 45^\circ$). The sharp structures at $B \approx 4.5 \text{ T}$ are electron spin resonances labeled by their subband indices $i=0,1$. The insert shows effective Landé factors in these two electric subbands. The arrow indicates the corresponding bulk value of n -type InSb.

The corresponding magnetic field in bulk n -type InSb ($n = 6 \times 10^{15} \text{ cm}^{-3}$) is $B = 4.13 \text{ T}$ at the same laser energy $\hbar\omega = 10.4 \text{ meV}$.⁵² The two broad maxima at lower magnetic fields are caused by cyclotron resonance that is split in tilted magnetic fields.⁵³ These maxima change their position with tilt angle whereas electron spin resonance does not within the precision of the experiments.

The line shapes of the electron spin resonances exhibit astonishing behavior. At a low electron density $n_s \approx 1.6 \times 10^{11} \text{ cm}^{-2}$ a “dip” is observed. This gradually evolves into a “peak” at the density $n_s \approx 2.8 \times 10^{11} \text{ cm}^{-2}$. This peak can be observed up to the density $n_s \approx 6 \times 10^{11} \text{ cm}^{-2}$. At densities $n_s \gtrsim 4 \times 10^{11} \text{ cm}^{-2}$ a second maximum is observed at slightly lower magnetic fields. The two maxima are attributed to electron spin resonance in the ground and first excited subband ($i=0,1$).

The profiles in the ground subband are Fano-type resonances.⁵⁴ However, we cannot extract Fano line-shape parameters since this would require frequency-domain studies. Until now, this is experimentally not possible, because of the extremely low absorption ($\Delta T/T \leq 0.1\%$). Generally, Fano profiles indicate interaction between a continuum of states and a discrete state. The profiles change, when the interaction between the continuum and the discrete state changes. At present, we cannot develop a detailed model, since this would require detailed knowledge of the surface band structure and cyclotron resonance in tilted magnetic fields. This is not yet fully known and we can only speculate, that the Fano continuum is represented by cyclotron transitions, whereas elec-

tron spin resonance acts as the discrete transition.

From the resonance structures, effective Landé g factors were extracted. The resonance magnetic fields are taken at the minimum of a dip and at the maximum of a peak. Effective Landé factors of the first two subbands are presented in the insert in Fig. 12. The Landé factor of the first excited subband is higher than the one of the ground subband. As is also expected from nonparabolicity, the Landé factors in both subbands decrease with increasing density.

V. SUMMARY

We have studied magneto-optical properties of the quasi-two-dimensional electron system in inversion layers on the narrow-gap semiconductor InSb with an emphasis on nonparabolicity, polaron effects, and electric dipole-induced electron spin resonance. The narrow-gap situation leads to small effective masses and to small densities of states in the electric subbands on this material. As a consequence, four subbands are occupied at densities $n_s \gtrsim 2 \times 10^{12} \text{ cm}^{-2}$ as has been determined from Shubnikov–de Haas measurements.

Nonparabolicity of the subband structure has various interesting consequences. The mass in a particular subband increases with inversion electron density. The masses and their increase are different in different subbands. This leads to distinct cyclotron resonances and allows the extraction of subband masses from far-infrared spectra obtained in magnetic or dispersive spectroscopy. Effective masses up to $m^* = 0.035m_e$ are obtained in the ground subband at an inversion electron density $n_s = 3 \times 10^{12} \text{ cm}^{-2}$ and low magnetic fields. As a result of nonparabolicity, subband masses also increase with cyclotron energy, except when the Fermi energy by far exceeds the cyclotron energy ($E_F \gg \hbar\omega_c$).

The subband structure in a magnetic field perpendicular to the surface could not be analyzed in all details. This means, we cannot give the transition energy of each spin-

split Landau transition $n^\pm \rightarrow (n+1)^\pm$ in a wider range of magnetic fields and electron densities. There are two reasons for this. In magnetic spectroscopy at a particular inversion electron density, the magnetic field does not only determine the cyclotron energy but also the occupancies of the initial and final Landau levels. Thus a particular transition cannot be studied independently as a function of magnetic field and inversion electron density. Secondly, in dispersive spectroscopy not all transitions that are possible could be resolved experimentally even with samples that show peak mobilities up to $5 \times 10^4 \text{ cm}^2 \text{ V}^{-1} \text{ s}^{-1}$.

We have observed magnetopolarons at cyclotron energies close to the reststrahlen band. We find that this resonant polaron effect is enhanced as compared to the bulk case as a result of the spatial confinement of the wave function in the inversion layer. Effects of screening of the polar interaction in the degenerate quasi-two-dimensional electron system and effects of interface or 2D optical phonons do not seem to be important on InSb.⁵⁵

Electron spin resonance could be studied in tilted magnetic fields. Fano-like line shapes are observed that indicate interaction of cyclotron resonance and electron spin resonance in tilted magnetic fields. As a result of nonparabolicity, the effective Landé factors increase with subband index and decrease with inversion electron density.

Qualitatively, our experiments can be explained by a three-level model in the triangular-well approximation of the electrostatic potential. However, to enable quantitative comparison with theory more realistic self-consistent Hartree calculations in quantizing magnetic fields are highly desirable for narrow-gap semiconductors like InSb.

ACKNOWLEDGMENTS

We thank F. Koch, S. Das Sarma, and W. Zawadzki for fruitful discussions and acknowledge financial support of the Deutsche Forschungsgemeinschaft (Bonn, Germany).

*Present address: VALVO RHW der Philips GmbH, Stresemannallee 101, D-2000 Hamburg 54, Federal Republic of Germany.

¹For a comprehensive review see T. Ando, A. B. Fowler, and F. Stern, *Rev. Mod. Phys.* **54**, 437 (1982).

²G. Abstreiter, J. P. Kotthaus, J. F. Koch, and G. Dorda, *Phys. Rev. B* **14**, 2480 (1976).

³H. Schaber and R. E. Doezema, *Phys. Rev. B* **20**, 5257 (1979).

⁴J. C. Maan, *Int. J. Infrared Millimeter Waves* **8**, 387 (1983).

⁵C. R. Pidgeon, in *Handbook on Semiconductors*, edited by T. S. Moss (North-Holland, Amsterdam, 1980), Vol. 2, Chap. 5, pp. 223–328.

⁶A. Därr and J. P. Kotthaus, *Surf. Sci.* **73**, 549 (1978).

⁷A. Därr, A. Huber, and J. P. Kotthaus, in *Physics of Narrow-Gap Semiconductors*, edited by J. Rauluszkiwicz, M. Górka, and E. Kaczmarek (PWN, Polish Scientific, 1978), pp. 417–422.

⁸D. C. Tsui, Th. Englert, A. Y. Cho, and A. C. Gossard, *Phys. Rev. Lett.* **44**, 341 (1980).

⁹S. Komiyama, H. Eyferth, and J. P. Kotthaus, *J. Phys. Soc. Jpn. Suppl. A* **49**, 687 (1980).

¹⁰D. H. Dickey, E. J. Johnson, and D. M. Larsen, *Phys. Rev. Lett.* **18**, 599 (1967).

¹¹M. Horst, U. Merkt, and J. P. Kotthaus, *Phys. Rev. Lett.* **50**, 754 (1983).

¹²H. Sigg, H. J. A. Bluysen, and P. Wyder, *Solid State Commun.* **48**, 897 (1983).

¹³M. Horst, U. Merkt, W. Zawadzki, J. C. Maan, and K. Ploog, *Solid State Commun.* **53**, 403 (1985).

¹⁴H. Sigg, P. Wyder, and J. A. A. J. Perenboom, *Phys. Rev. B* **31**, 5253 (1985).

¹⁵E. Preuss, *Phys. Rev. B* **1**, 3392 (1970).

¹⁶N. Kotera, Y. Katayama, and K. F. Komatsubara, *Phys. Rev. B* **5**, 3065 (1972).

¹⁷A. Därr, J. P. Kotthaus, and J. F. Koch, *Solid State Commun.* **17**, 455 (1975).

¹⁸A. Därr, J. P. Kotthaus, and T. Ando, in *Physics of Semiconductors*, edited by F. G. Fumi (North-Holland, Amsterdam,

- 1976), pp. 774–777.
- ¹⁹W. Beinvoogl and J. F. Koch, *Solid State Commun.* **24**, 687 (1977).
- ²⁰K. Wiesinger, W. Beinvoogl, and F. Koch, in *Physics of Semiconductors*, edited by B. L. H. Wilson (Institute of Physics, London, 1979), pp. 1215–1218.
- ²¹Y. Takada, K. Arai, N. Uchimura, and Y. Uemura, *J. Phys. Soc. Jpn.* **49**, 1851 (1980).
- ²²Y. Takada, *J. Phys. Soc. Jpn.* **50**, 1998 (1981).
- ²³G. E. Marques and L. J. Sham, *Surf. Sci.* **113**, 131 (1982).
- ²⁴W. Zawadzki, *J. Phys. C* **16**, 229 (1983).
- ²⁵W. Zawadzki, in *Two-Dimensional Systems, Heterostructures, and Superlattices*, edited by G. Bauer, F. Kuchar, and H. Heinrich (Springer, Berlin, 1984), pp. 2–11.
- ²⁶A. D. Wieck, E. Batke, D. Heitmann, J. P. Kotthaus, and E. Bangert, *Phys. Rev. Lett.* **53**, 493 (1984).
- ²⁷M. Horst, U. Merkt, and K. G. Germanova, *J. Phys. C* **18**, 1025 (1985).
- ²⁸W. Kiefer, W. Richter, and M. Cardona, *Phys. Rev. B* **12**, 2346 (1975).
- ²⁹E. Liarokapis and E. Anastassakis, *Phys. Rev. B* **30**, 2270 (1984).
- ³⁰S. J. Allen, Jr., D. C. Tsui, and F. DeRosa, *Phys. Rev. Lett.* **35**, 1359 (1975).
- ³¹H. C. Gatos and M. C. Lavine, *J. Phys. Chem. Solids* **14**, 169 (1960).
- ³²U. Mackens and U. Merkt, *Thin Solid Films* **97**, 53 (1982).
- ³³V. Dolgoplov, C. Mazuré, A. Zrenner, and F. Koch, *J. Appl. Phys.* **55**, 4280 (1984).
- ³⁴E. Batke and D. Heitmann, *Infrared Phys.* **24**, 189 (1984).
- ³⁵A. Därr, Dissertation, Technische Universität München, 1978 (unpublished).
- ³⁶M. Horst, U. Merkt, and J. P. Kotthaus, *Surf. Sci.* **113**, 315 (1982).
- ³⁷J. R. Apel, T. O. Poehler, C. R. Westgate, and R. I. Joseph, *Phys. Rev. B* **4**, 436 (1971).
- ³⁸S. Das Sarma and A. Madhukar, *Phys. Rev. B* **22**, 2823 (1980).
- ³⁹E. D. Palik and G. B. Wright, in *Semiconductors and Semimetals*, edited by R. K. Willardson and A. C. Beer (Academic, New York, 1967), Vol. 3, pp. 421–458.
- ⁴⁰A. Gold, *Phys. Rev. B* **32**, 4014 (1985), and references therein.
- ⁴¹S. Das Sarma and B. A. Mason, *Ann. Phys. (N.Y.)* **163**, 78 (1985), and (private communication).
- ⁴²D. M. Larsen, *Phys. Rev. B* **30**, 4595 (1984).
- ⁴³F. M. Peeters and J. T. Devreese, *Phys. Rev. B* **31**, 3689 (1985).
- ⁴⁴G. Lindemann, W. Seidenbusch, R. Lassnig, J. Edlinger, and E. Gornik, *Physica* **117B&118B**, 649 (1983); G. Lindemann, R. Lassnig, W. Seidenbusch, and E. Gornik, *Phys. Rev. B* **28**, 4693 (1983).
- ⁴⁵J. Scholz, F. Koch, J. Ziegler, and H. Maier, *Solid State Commun.* **46**, 665 (1983).
- ⁴⁶R. J. Nicholas, L. C. Brunel, S. Huant, K. Karrai, J. C. Portal, M. A. Brummell, M. Razeghi, K. Y. Cheng, and A. Y. Cho, *Phys. Rev. Lett.* **55**, 883 (1985).
- ⁴⁷S. Das Sarma, *Phys. Rev. Lett.* **52**, 859 (1984); **52**, 1570(E) (1984).
- ⁴⁸S. Das Sarma and B. A. Mason, *Phys. Rev. B* **31**, 5536 (1985); S. Das Sarma, *ibid.* **27**, 2590 (1983); **31**, 4034(E) (1985).
- ⁴⁹R. Lassnig and W. Zawadzki, *Surf. Sci.* **142**, 388 (1984).
- ⁵⁰W. Xiaoguang, F. M. Peeters, and J. T. Devreese, *Phys. Status Solidi B* **133**, 229 (1986).
- ⁵¹S. Gopalan, J. K. Furdyna, and S. Rodriguez, *Phys. Rev. B* **32**, 903 (1985).
- ⁵²B. D. McCombe and R. J. Wagner, *Phys. Rev. B* **4**, 1285 (1971).
- ⁵³J. H. Crasemann and U. Merkt, *Solid State Commun.* **47**, 917 (1983).
- ⁵⁴U. Fano, *Phys. Rev.* **124**, 1866 (1961).
- ⁵⁵M. Horst and U. Merkt, *Solid State Commun.* **54**, 559 (1985).